Investigating the Prevalence of Complex Fiber Configurations in White Matter Tissue with Diffusion Magnetic Resonance Imaging

Ben Jeurissen,[1]* Alexander Leemans,[2] Jacques-Donald Tournier,[3] Derek K. Jones,[4,5] and Jan Sijbers[1]

[1]*IBBT- Vision Lab, Department of Physics, University of Antwerp, Belgium*
[2]*Image Sciences Institute, University Medical Center Utrecht, The Netherlands*
[3]*Brain Research Institute, Florey Neuroscience Institutes, Melbourne, Australia*
[4]*CUBRIC, School of Psychology, Cardiff University, Cardiff, United Kingdom*
[5]*Neuroscience and Mental Health Research Institute, Cardiff University, Cardiff, United Kingdom*

◆ ━━━━━━━━━━━━━━━━━━━━━━━━━━━━━━━━━━━━━ ◆

Abstract: It has long been recognized that the diffusion tensor model is inappropriate to characterize complex fiber architecture, causing tensor-derived measures such as the primary eigenvector and fractional anisotropy to be unreliable or misleading in these regions. There is however still debate about the impact of this problem in practice. A recent study using a Bayesian automatic relevance detection (ARD) multicompartment model suggested that a third of white matter (WM) voxels contain crossing fibers, a value that, whilst already significant, is likely to be an underestimate. The aim of this study is to provide more robust estimates of the proportion of affected voxels, the number of fiber orientations within each WM voxel, and the impact on tensor-derived analyses, using large, high-quality diffusion-weighted data sets, with reconstruction parameters optimized specifically for this task. Two reconstruction algorithms were used: constrained spherical deconvolution (CSD), and the ARD method used in the previous study. We estimate the proportion of WM voxels containing crossing fibers to be ~90% (using CSD) and 63% (using ARD). Both these values are much higher than previously reported, strongly suggesting that the diffusion tensor model is inadequate in the vast majority of WM regions. This has serious implications for downstream processing applications that depend on this model, particularly tractography, and the interpretation of anisotropy and radial/axial diffusivity measures. *Hum Brain Mapp 34:2747–2766, 2013.* © 2012 **Wiley** Periodicals, Inc.

Key words: high-angular resolution diffusion imaging; white matter; partial volume effect; crossing fibers; constrained spherical deconvolution; residual bootstrap; bedpostx

◆ ━━━━━━━━━━━━━━━━━━━━━━━━━━━━━━━━━━━━━ ◆

*Correspondence to: Ben Jeurissen, Vision Lab, Department of Physics, University of Antwerp, Universiteitsplein 1, B-2610 Wilrijk, Belgium. E-mail: ben.jeurissen@ua.ac.be

INTRODUCTION

Diffusion-weighted (DW) magnetic resonance imaging (MRI) is a unique noninvasive method for probing tissue microstructure in vivo, based on the random thermal motion of water molecules [Stejskal and Tanner, 1965]. Currently, it is amongst the most popular imaging techniques for assessing brain tissue microstructure, particularly in white matter (WM) [Assaf and Pasternak, 2008]. Within the WM, fiber orientations can be extracted from the DW signal, opening up new avenues for investigating brain connectivity in vivo using so-called fiber-tracking algorithms [Jones, 2008]. The ability to assess WM microstructure and pathways of the whole brain from in vivo scans raises possibilities for clinical applications, and there has been a rapid increase in clinical studies using DW MRI-derived indices [Mori and Zhang, 2006] and fiber tractography [Ciccarelli et al., 2008; Johansen-Berg and Behrens, 2006].

Currently, diffusion tensor imaging (DTI) is the established method for assessing WM microstructure and connectivity [Basser et al., 1994a,b; Mori and van Zijl, 2002]. However, in voxels containing multiple fiber orientations, this model has been shown to be inadequate [Alexander et al., 2001, 2002; Frank, 2001, 2002; Tuch et al., 2002]. Such voxels occur frequently throughout the WM due to partial volume effects between adjacent tracts. This has important implications for DTI-based fiber tractography, as most WM tracts will traverse regions with multiple fiber orientations at some point along their path. In such regions, the orientation extracted from the diffusion tensor is unreliable and may cause false negatives, in which tracking terminates [Behrens et al., 2007; Jeurissen et al., 2011], or false positives, in which tracking switches to an unrelated adjacent tract [Jeurissen et al., 2011; Pierpaoli et al., 2001]. It also complicates the interpretation of DTI-derived diffusion indices such as fractional anisotropy (FA), which are often suggested for use as surrogate markers of WM "integrity" [Jones and Cercignani, 2010; Vos et al., 2011, 2012; Wheeler-Kingshott and Cercignani, 2009].

Remarkably, the question of what proportion of WM voxels is affected by crossing fibers remains to be addressed in a robust and satisfactory manner. With recent advances in high-angular resolution diffusion imaging (HARDI) [Tuch et al., 2002], it is now possible to reliably extract fiber orientations in regions of increased complexity [Alexander, 2006; Tournier et al., 2011]. Although a number of studies have attempted to classify voxels according to the complexity of the fiber arrangement, many do not report the proportion of affected voxels, and all of them are likely to seriously underestimate the extent of the problem, for a number of reasons outlined below. Early studies distinguished between voxels with isotropic, single-fiber, and multifiber characteristics based on the shape of the ADC profile and have reported clustered and symmetric regions of increased complexity, supporting genuine effects consistent with anatomical knowledge

[Alexander et al., 2002; Frank, 2002]. More recently, a Bayesian automatic relevance determination (ARD) method was proposed to infer the number of fiber orientations in a multicompartment model [Behrens et al., 2007]; using 60 diffusion gradient orientations and a b-value of $b = 1000$ s/mm^2, the model evidence was sufficiently strong to support the presence of more than one fiber orientation in one third of the voxels with FA > 0.1. However, nowhere in the brain was the model evidence sufficiently strong to support the presence of more than two fiber orientations. In another study, Q-Ball imaging was used in conjunction with bootstrapping to estimate the probability of different numbers of fiber populations existing in different brain tissues [Haroon et al., 2009]. This study used 61 diffusion gradient orientations with a slightly higher b-value of $b = 1200$ s/mm^2. Although the authors did not explicitly assess the number of voxels containing multiple fiber orientations, their results seem to indicate that only a small proportion of WM voxels are affected by partial volume effects and that clustered regions with a high probability of more than two fiber orientations cannot be found. These recent studies are likely to be grossly underpowered for estimating the proportion of crossing fiber voxels (a task that they were not specifically designed to do). On the other hand, there are suggestions in other recent publications that voxels with multiple fiber orientations are actually commonly encountered [Descoteaux et al., 2009; Jeurissen et al., 2011]. It is clear therefore that a reliable estimate of the proportion of affected voxels remains to be provided.

Given the implications that this might have for DTI-based tractography and the interpretation of DTI-derived diffusion indices, in this study, we set out *specifically* to estimate the extent of the crossing fiber problem as well as its likely impact on tensor-based analyses. For this purpose, we acquired large, high-quality DW data sets (using a twice-refocused and cardiac-gated sequence) consisting of 720 DW images, roughly 12 times the amount of data that was used in previous studies, with a correspondingly much higher power to detect the effects of interest [Jones, 2004]. For each voxel, the fiber orientations and their respective volume fractions were extracted using two different, readily available approaches: constrained spherical deconvolution (CSD) [Tournier et al., 2007] and the bedpostx algorithm which implements the ARD method mentioned previously [Behrens et al., 2007] and is distributed as part of the FSL [Woolrich et al., 2009]. In both cases, parameters of the reconstruction were tuned specifically to ensure reliable estimates given our particular acquisition parameters. Based on these data, we report the proportion of multifiber voxels detected within the WM and their orientations. To assess the impact of these voxels on tensor-derived tractography analyses, we also report the angular error between the fiber orientations estimated using CSD and DTI. Finally, to assess the impact on the interpretation of tensor-derived scalar measures, we report the volume fraction of each voxel taken up by secondary or tertiary
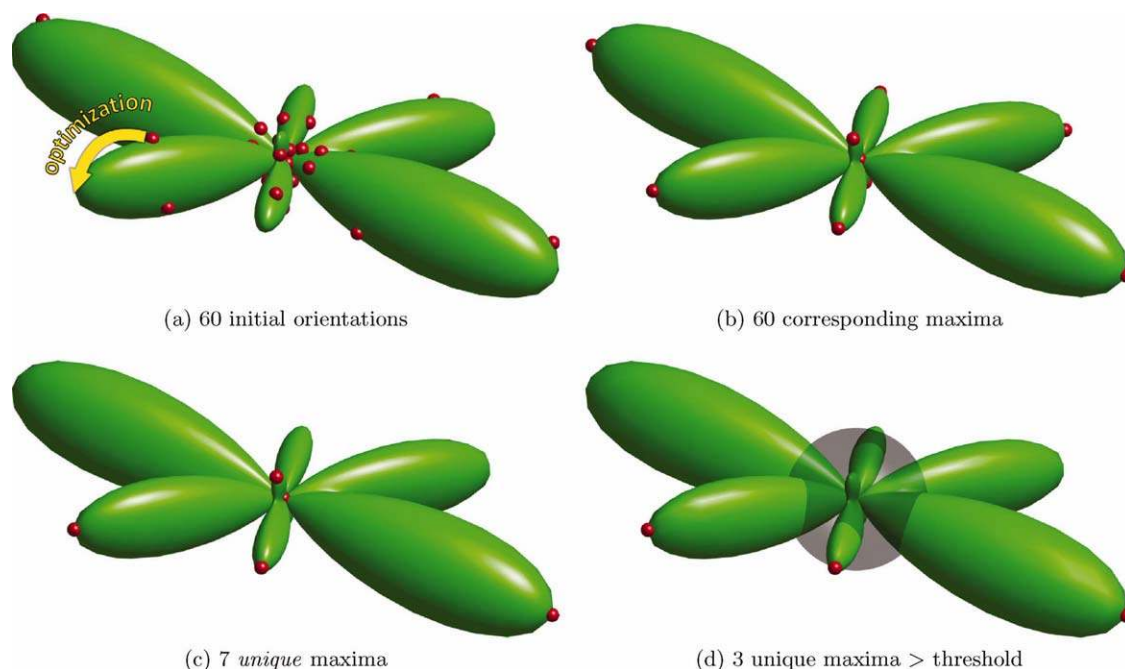
(a) 60 initial orientations

(b) 60 corresponding maxima

(c) 7 *unique* maxima

(d) 3 unique maxima > threshold

Figure 1.

Extraction of the CSD FOD fiber orientations: three orientation example. (**a**) Points uniformly distributed on the half-sphere (red dots) used as starting points for the maximization of the FOD amplitude (green); (**b**) the corresponding FOD maxima (note that many overlap); (**c**) the unique FOD maxima (note that three of the spurious maxima have very low amplitude and are clustered near the origin); (**d**) FOD maxima with amplitude higher than FOD threshold (gray sphere). [Color figure can be viewed in the online issue, which is available at wileyonlinelibrary.com.]

fiber orientations, whose presence would confound such measures.

MATERIALS AND METHODS

Overview

To estimate the impact of multifiber voxels on DTI, it is first necessary to obtain robust estimates of the fiber orientations and their respective volume fractions within each WM voxel. To achieve this requires both high-quality DW data and robust fiber orientation estimation strategies. To this end, our approach involved: the acquisition of very high quality in vivo data sets; extensive simulations to select optimal reconstruction parameters tuned specifically for these data sets; and the application of the resulting optimized reconstruction algorithms to the in vivo data sets. These steps are described in detail in the following sections. We first provide a brief overview of both fiber estimation methods to emphasize which reconstruction parameters are needed to be tuned for this study.

Fiber Orientation Estimation Using CSD

The procedure used to estimate fiber orientations using CSD [Tournier et al., 2007] involved first deconvolving the single-fiber "response function" (described below) from the DW signal to obtain the fiber orientation distribution (FOD), with maximum harmonic degree $L = 8$ [Tournier et al., 2007], followed by a peak-finding procedure to identify distinct orientations. Finally, fiber orientations were only considered if the amplitude of the corresponding peak in the FOD exceeded a threshold specifically tuned for this study (see below for details). An example of this procedure for a voxel with three fiber orientations is shown in Figure 1.

The single-fiber response function corresponds to the DW signal that would be expected for an ideal fiber population aligned along the z-axis and was estimated from the data themselves using a previously published approach [Tournier et al., 2004, 2007]. In brief, WM voxels with FA > 0.7 were identified, and, in each of these voxels, the DW signal was reoriented such that the orientation of the major eigenvector of the diffusion tensor was aligned with the z-axis. The spherical harmonic (SH) decompositions of all the resulting profiles were then averaged to provide a robust estimate of the true response function. To constrain the response function to an axially symmetric function, only SH coefficients with order $m = 0$ were estimated [Tournier et al., 2004].

The peak-finding procedure consisted of a Newton optimization algorithm, started from a dense set of equally

distributed spherical sample points to find the local maxima of the FOD (duplicate local maxima were excluded). The number of unique peak FOD orientations with amplitude above threshold was counted and assumed to be equal to the number of fiber orientations. In this study, voxels containing more than three orientations will be reported as containing ≥ 3 orientations.

Fiber Orientation Estimation Using Bedpostx

The procedure used to estimate fiber orientations using ARD was performed using the FSL tool *bedpostx* [Behrens et al., 2007], which we describe briefly here. Bedpostx uses a Bayesian framework to estimate local probability density functions on the parameters of a multicompartment model. Using ARD, the method performs online selection of the number of fiber orientations supported by the data at each voxel by forcing the fiber volume fractions to take the value zero if, and only if, there is no evidence in the data for their existence [Behrens et al., 2007]. The maximum number of fiber orientations allowed in the multicompartment model was set to 3. To extract the number of fiber orientations in each voxel, we thresholded the volume fractions at 0.05, as in Behrens et al. [2007].

Bedpostx uses a Monte Carlo Markov Chain algorithm to infer on the parameters of the model. In this study, we used a modified burn-in period of 10,000 iterations, as the default value of 1,000 was found to be insufficient to ensure convergence of the Markov chains in a significant proportion of runs [Miller et al., 2011; O'Muircheartaigh et al., 2011].

Data Acquisition and Preprocessing

Both DW and T_1-weighted images were acquired on a General Electric (Milwaukee, WI) 3T HDx Signa system with an eight-channel receive-only head coil. The experiment was repeated on two different healthy adult volunteers. Both subjects gave written informed consent to participate in this study under a protocol approved by the Cardiff University School of Psychology Ethics Committee.

Each subject was scanned 12 times using a twice-refocused spin-echo EPI sequence with TE = 86 ms and $2.4 \times 2.4 \times 2.4$-mm^3 voxel size (FOV 23×23 cm^2, 96×96 acquisition matrix, NEX = 1, partial Fourier encoding with 16 overscans, 60 axially acquired slices with 2.4 mm thickness with no gap, ASSET factor = 2). Diffusion gradients were applied in 60 directions uniformly distributed on a sphere through electrostatic repulsion with $b = 1200$ s/mm^2 [Jones et al., 1999]. For each scan, six images with $b = 0$ s/mm^2 were also acquired. To avoid pulsation artifacts, cardiac gating was applied using a peripheral pulse oximeter with an effective TR = 20 R–R intervals. Signal-to-noise ratio (SNR) within all WM voxels of the $b = 0$ s/mm^2 images was on average 24.9 with a standard deviation of 6.1 [Dietrich et al., 2007]. In addition, each subject was

scanned with a 3D fast-spoiled gradient echo sequence with TR/TE = 7.9/3.0 ms and $1 \times 1 \times 1$-mm^3 voxel size (FOV = $256 \times 256 \times 176$ mm^3, $256 \times 256 \times 176$ acquisition matrix, TI = 450 ms, flip angle = $20°$, NEX = 1) to produce an anatomical T_1-weighted image.

For each subject, all DW scans were concatenated (not averaged) into a single data set and corrected for subject motion and residual eddy current induced geometric distortions with the required B-matrix adjustments [Leemans and Jones, 2009], resulting in a total of 720 DW and 72 $b = 0$ s/mm^2 images per subject. The tensor model was fitted to the motion-corrected data using a constrained nonlinear regression method [Koay et al., 2006] and, subsequently, mean diffusivity (MD) and FA were calculated from the tensor's eigenvalues. Glyph visualization was done with *ExploreDTI* [Leemans et al., 2009].

Optimization of Reconstruction Parameters

Although the SNR dependencies of both CSD and bedpostx have previously been studied in great detail [Behrens et al., 2007; Tournier et al., 2007, 2008]; in this study, additional experiments were performed to select optimal reconstruction parameters tuned *specifically* for the data sets used in this study. For this purpose, extensive simulations were performed using parameters measured from the real data themselves to determine the most suitable reconstruction parameters to use for each method and hence ensure optimal detection of fiber orientations given our particular acquisition parameters.

These simulations were performed as follows. First, noise-free DW data were generated for voxels assumed to contain a number (1, 2, or 3) of fiber orientations, by combining DW signals generated assuming axially symmetric diffusion tensor profiles for each fiber population [Leemans et al., 2005], with interfiber angles ranging from $90°$ to $10°$. The eigenvalues of the constituent tensors were set to $[1.7\ 0.3\ 0.3] \times 10^{-3}$ mm^2/s, corresponding to the average values found in the midsagittal area of the splenium of the corpus callosum in the real data sets. The same gradient directions and b-value were used as in the real data acquisition. Next, Rician noise was added using SNR = 15, corresponding to the lower end of the range of SNR values measured in the real data sets, and the number of fiber orientations was estimated from the resulting noisy simulated data using both CSD and bedpostx. This procedure was repeated for 1,000 Rician noise instances.

For both CSD and bedpostx, outcome was measured as the proportion of false positives, defined as any simulated run where the number of estimated fiber orientations was greater than the actual number simulated. For CSD, the reconstruction parameter of interest was the threshold on the FOD peak amplitude used to identify distinct orientations (see earlier). For bedpostx, the reconstruction parameter of interest was the ARD weight, with higher weights resulting in fewer secondary fibers per voxel. For both

methods, the smallest reconstruction parameter that resulted in *zero* false positives was used for the analysis of the in vivo data. The minimum resolvable angle of both methods (i.e., the interfiber angle at which the correct number of fiber orientations can still be reliably estimated) was also assessed using these simulations for a range of volume fractions.

In Vivo Estimation of Fiber Orientations

To estimate the fiber orientations and their respective volume fractions over all WM voxels, both CSD and bedpostx methods were applied to the real data sets of both subjects, using the procedures described in the previous corresponding sections, and the conservative reconstruction parameters specifically tuned in the simulations above. To avoid partial volume effects with isotropic compartments, such as gray matter (GM) and cerebrospinal fluid (CSF), the analysis was restricted to voxels within a pure WM mask, derived from the T_1-weighted images. The T_1-derived WM mask was generated as follows. First, a tissue probability map was estimated from the T_1-weighted image (Fig. 2a) using the unified segmentation tool from SPM [Ashburner and Friston, 2005] (Fig. 2b). Next, the T_1-weighted image was registered to the FA image using 3D nonrigid *b*-spline-based registration with Mattes mutual information as the similarity measure [Klein et al., 2010; Mattes et al., 2001] (Fig. 2d). The derived transform was then used to warp the WM probability map from the T_1-weighted image to the diffusion images, allowing easy identification of WM voxels inside the DW volume. To restrict the study to pure WM voxels only, a binary WM mask was created by selecting all voxels with WM probability higher than 95% (Fig. 2c). Finally, a small number of voxels at the edges of the WM mask were removed, because they were found to contain high MD values resulting from partial voluming with CSF (as indicated by the red voxels in Fig. 2c). These outliers were identified using the criterion MD > median (MD) + 1.5 * IQR (MD) (where IQR is the interquartile range over the whole mask).

In addition, the reproducibility of the CSD reconstruction was assessed using a residual bootstrap approach, described previously [Jeurissen et al., 2011]. One thousand residual bootstrap realizations of the entire data set were generated, using a SH model with maximum harmonic degree $L = 8$ [Jeurissen et al., 2011]. Unfortunately, it was not possible to perform the equivalent experiments for bedpostx due to its prohibitively long processing times.

To further illustrate the "global" consistency of the multifiber voxels, a fiber tractography technique was used, based on the CSD FOD maxima [Fillard et al., 2011; Jeurissen et al., 2009, 2011]. The step size was set to 0.2 mm. Tracking was terminated when the extracted FOD orientation amplitude dropped below the same threshold that was used for the fiber orientation extraction, or when the

angle between two successive steps exceeded 10°. A seed ROI was placed in a region with more than two fiber orientations. Tract visualization was performed with the *ExploreDTI* diffusion MRI toolbox [Leemans et al., 2009].

The effect of using different values for the threshold on the FOD amplitude (for CSD) and the partial volume fractions (for bedpostx) was also investigated. This was done by plotting the proportion of WM voxels estimated as containing 1, 2, or ≥ 3 fiber orientations as a function of these thresholds. Finally, both fiber orientation estimation methods are limited by their minimum detectable crossing angle; the angle at which fibers cross will therefore have an impact on the results. This issue was examined by plotting a histogram of the interfiber angle over all voxels.

Assessment of Impact on DTI

To assess the practical impact of these findings for tractography or anisotropy analyses, two further analyses were performed. Tractography analyses will obviously be affected by errors in the estimated fiber orientations. Therefore, the angle between the fiber orientations estimated by the primary eigenvector of the diffusion tensor, and the nearest peak to this direction in the CSD FOD was measured in each voxel and displayed both as a map and as a histogram over all WM voxels. For anisotropy analyses, issues will arise if fibers with secondary or tertiary orientations take up a substantial volume fraction of the voxel. Therefore, the ratio of the volume fractions of the nondominant versus all fiber orientations was estimated in each WM voxel and displayed both as a map and using histograms.

RESULTS

Optimization of Reconstruction Parameters

Figure 3 demonstrates the need for an appropriate FOD threshold (for CSD) or ARD weight (for bedpostx) to remove spurious fiber orientations from the results. For CSD, the number of false positives dropped rapidly with increasing FOD threshold and was already below 1 in 1,000 with a threshold of 0.02. However, for false positives to be completely removed, a threshold of 0.1 was required. For bedpostx, the number of false positives dropped with increasing ARD weight and reached zero at a weight value of 10. These values (0.1 for the CSD FOD threshold, 10 for the ARD weight) were therefore used for all subsequent analyses, including the in vivo data analyses, unless otherwise stated.

The sensitivity of both methods with respect to volume fraction and interfiber angle is shown in Figure 4. As the interfiber angle dropped below $\sim 60°$, CSD FOD peaks started to merge to form a single peak, with merging occurring in almost all cases at an interfiber angle of $\sim 45°$; these would hence no longer be counted as separate
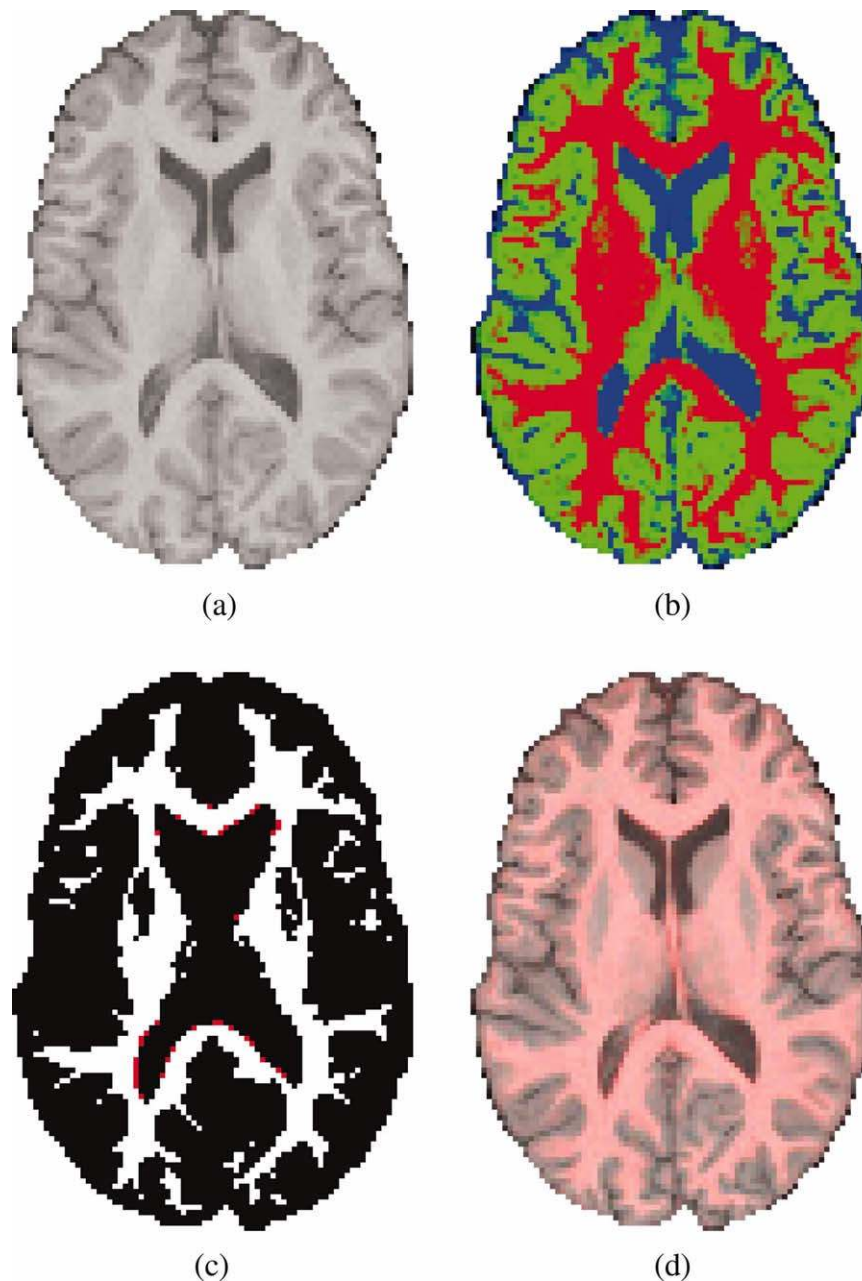
Figure 2.

Computation of the WM mask: T_1-weighted image (**a**) and the corresponding WM/GM/CSF segmentation (**b**). WM probability is colored red, GM probability green, and CSF probability blue. The WM probability map is thresholded at 95% to create a binary WM map (**c**). MD outliers resulting from partial volume effect at the interface between WM and CSF are colored red. Coregistered T_1-weighted image (gray) overlaid with FA image (pink) (**d**). [Color figure can be viewed in the online issue, which is available at wileyonlinelibrary.com.]

fiber orientations (Fig. 4a,c). On the other hand, bedpostx was unable to consistently report three-fiber orientations when three-fiber orientations were simulated, reporting one or two-fiber orientations instead (Fig. 4d), in agreement with earlier simulations performed in Behrens et al.

[2007]. For the two-fiber simulations (Fig. 4b), bedpostx performed similarly to CSD, although it failed to recover fibers with small volume fractions that could still be reliably detected using CSD. Note that while it is in theory possible to boost the minimum resolvable angle of
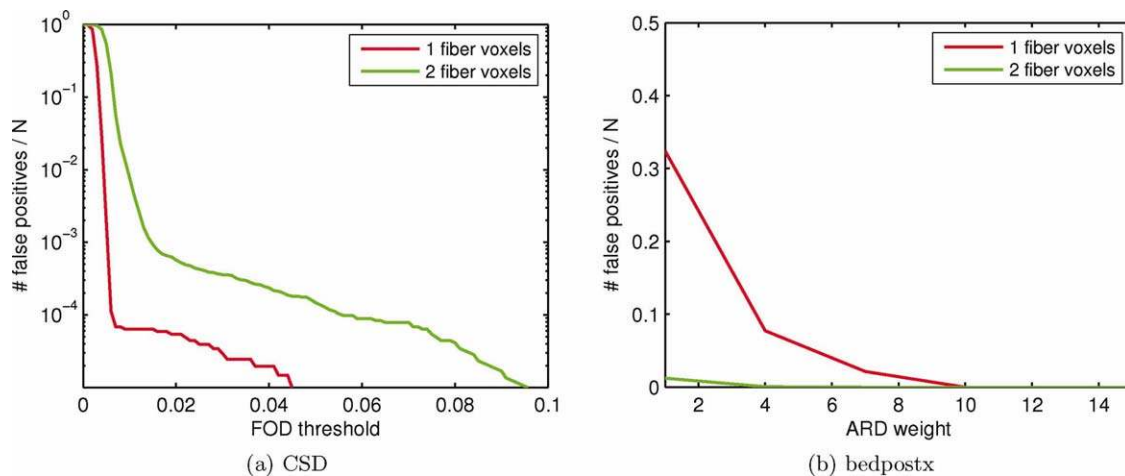
Figure 3.

Multifiber simulations (specificity): the relative number of false positives as a function of the CSD FOD threshold (**a**) and the bedpostx ARD weight (**b**) for one-fiber (red curve) and two-fiber (green curve) voxels. [Color figure can be viewed in the online issue, which is available at wileyonlinelibrary.com.]

bedpostx using a smaller ARD weight, this would result in an increased number of false positives (Fig. 3b).

In Vivo Estimation of Fiber Orientations

When applied to the in vivo data, both methods performed as predicted by the simulations. In voxels where CSD reports one or two fiber orientations, bedpostx usually reports the same number of fiber orientations, and the orientations are almost identical (Fig. 5), consistent with our simulation results (Fig. 4). In voxels where CSD reports ≥3 fiber orientations, bedpostx reports only one or two fiber orientations, again in agreement with the simulation results. Note that while these orientations constitute a subset of the orientations estimated using CSD in most voxels, in some cases, they are not consistent with those estimated using CSD. Note also that in voxels with three-fiber orientations, the CSD orientations are very coherent, showing continuous transitions with the surrounding orientations, even those corresponding to small FOD amplitudes (Fig. 5b).

The maps of the number of fiber populations detected (Fig. 6) and of their respective orientations (Figs. 7 and 8) both show a high degree of structural coherence and symmetry, supporting genuine anatomical features (Figs. 6–8). Note that these figures correspond to the results for subject 1 only; the results for subject 2 are broadly equivalent and provided as Supporting Information. Large, bilaterally symmetrical clusters of single-fiber voxels (colored in red) are found mainly in the largest bundles such as parts of the corpus callosum (CC, arrow 1), middle cerebellar peduncle (arrow 2), and the posterior limb of the internal capsule (arrow 3). Large clusters of voxels containing two orientations are also present, again symmetrically distributed throughout the brain. Examples of regions containing two-fiber orientations (colored in green) include the mixture of transverse pontine (oriented left–right) and motor (oriented inferior–superior) fibers (arrow 4) and the mixture of fibers from the superior longitudinal fasciculus (SLF; oriented anterior–posterior) and corona radiata (oriented inferior–superior) (arrow 5). Large clusters of voxels with ≥3 fiber populations (colored in blue) can also be found in the CSD results, for example, in the regions where fibers from the corona radiata (inferior–superior), SLF (anterior–posterior), and CC (left–right) interdigitate (arrow 6). In contrast, no consistent areas containing ≥3 orientations were observed in the bedpostx results: in those regions where CSD identified ≥3 orientations, bedpostx reported only one or two orientations, consistent with the simulation results (Fig. 4).

Table I summarizes the incidence of 1, 2, and ≥3 fiber orientations in all WM voxels. Using CSD, these were estimated to be ∼ 9, 46, and 45%, respectively; two or more fiber orientations were found in ∼ 90% of all WM voxels. Using bedpostx, these were estimated to be ∼ 37, 62, and 1%, respectively; in this case, complex fiber configurations were observed in ∼ 63% of all WM voxels.

Figure 9 shows the fiber orientations extracted using CSD from the individual bootstrap realizations in the crossing fiber region depicted in Figure 5b. To aid visibility, only 30 residual bootstrap realizations were plotted. Notice that the orientations are very clustered, indicating that the same fiber orientations are recovered consistently over bootstrap realizations, even in three-fiber voxels.

Figure 10 shows the CSD fiber tracking results when seeding in a three-fiber region. Notice how the locally extracted fiber orientations are globally consistent and
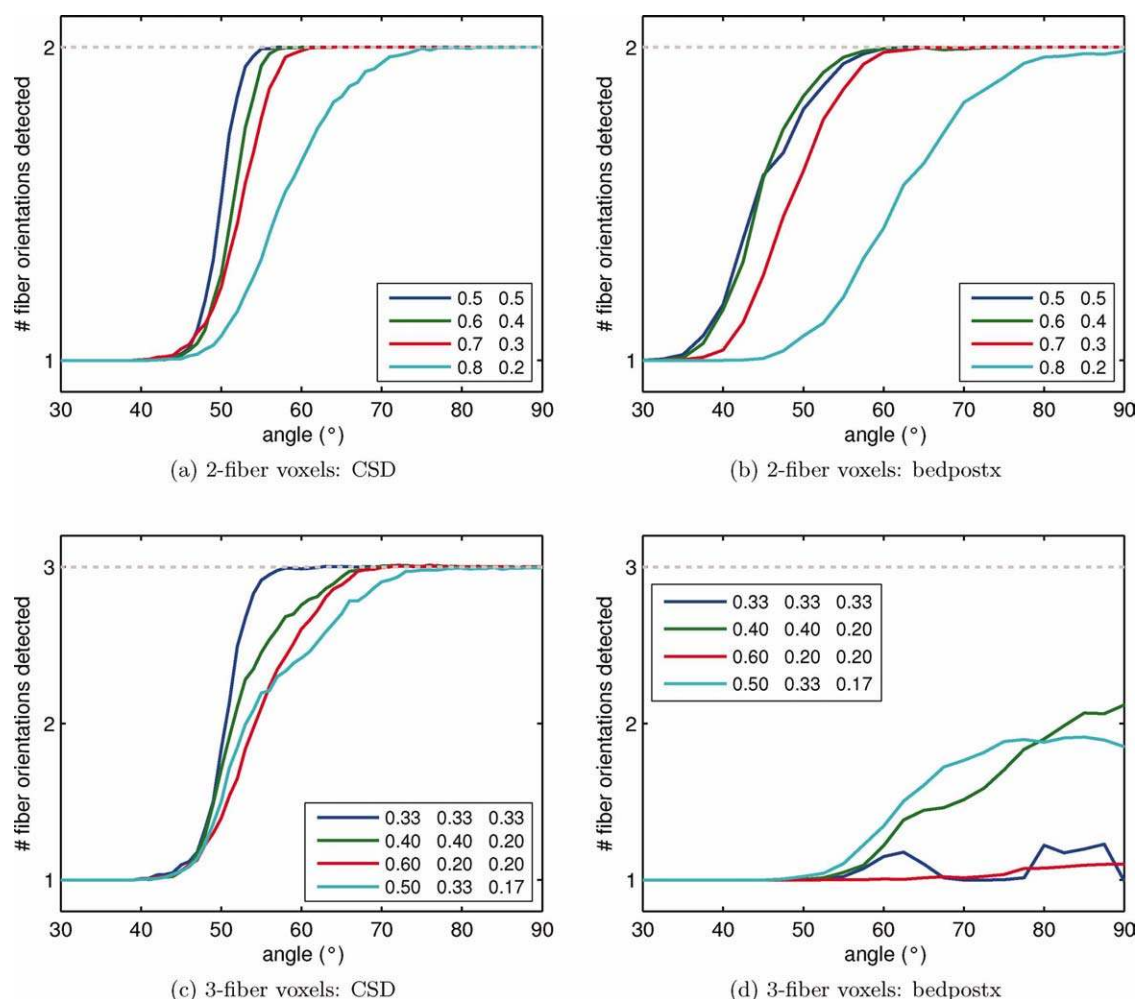
Figure 4.

Multifiber simulations (minimum resolvable angle). The average number of detected fiber orientations in two-fiber and three-fiber voxels as a function of angle. The different colors represent the different weights of the constituent DWI signals. [Color figure can be viewed in the online issue, which is available at wileyonlinelibrary.com.]

result in anatomically plausible fiber bundles. Commissural fibers from the CC are shown in red, association fibers from the arcuate fasciculus are colored green, and projection fibers from the corticospinal tract are shown in blue.

Using the residual bootstrap approach, we were also able to estimate the uncertainty in the percentages reported in Table I for the CSD case. The 95% confidence intervals for the percentage of 1, 2, and ≥3 fiber voxels were ±0.3%, ±0.5%, and ±0.7%, respectively, for subject 1, and ±0.6%, ±1.3%, and ±1.7%, respectively, for subject 2. These small confidence intervals demonstrate the reproducibility of our CSD results with these data sets.

The effect of the FOD threshold (for CSD) or the partial volume threshold (for bedpostx) is shown in Figure 11. As expected, an increase in the thresholds results in a reduc-

tion of the proportion of multifiber voxels for both approaches. For bedpostx, the results are relatively stable for partial volume thresholds between ∼ 0.01 and 0.1 (the actual value used was 0.05). By contrast, the CSD results do not show a region that is stable with respect to the FOD threshold. Initially, the proportion of ≥3 fiber voxels reduces while the proportion of two-fiber voxels increases, as would be expected. At an FOD threshold of ∼ 0.2, the proportion of both 2 and ≥3 fiber voxels reduces while that of single-fiber voxels increases. Importantly, even with a doubling of the FOD threshold to a value of 0.2 (actual value used was 0.1), the proportion of multifiber voxels is still very high at ∼ 78%.

The performance of both methods with respect to interfiber angle can be appreciated from the histograms shown in Figure 12. With CSD, a much higher number of 90°
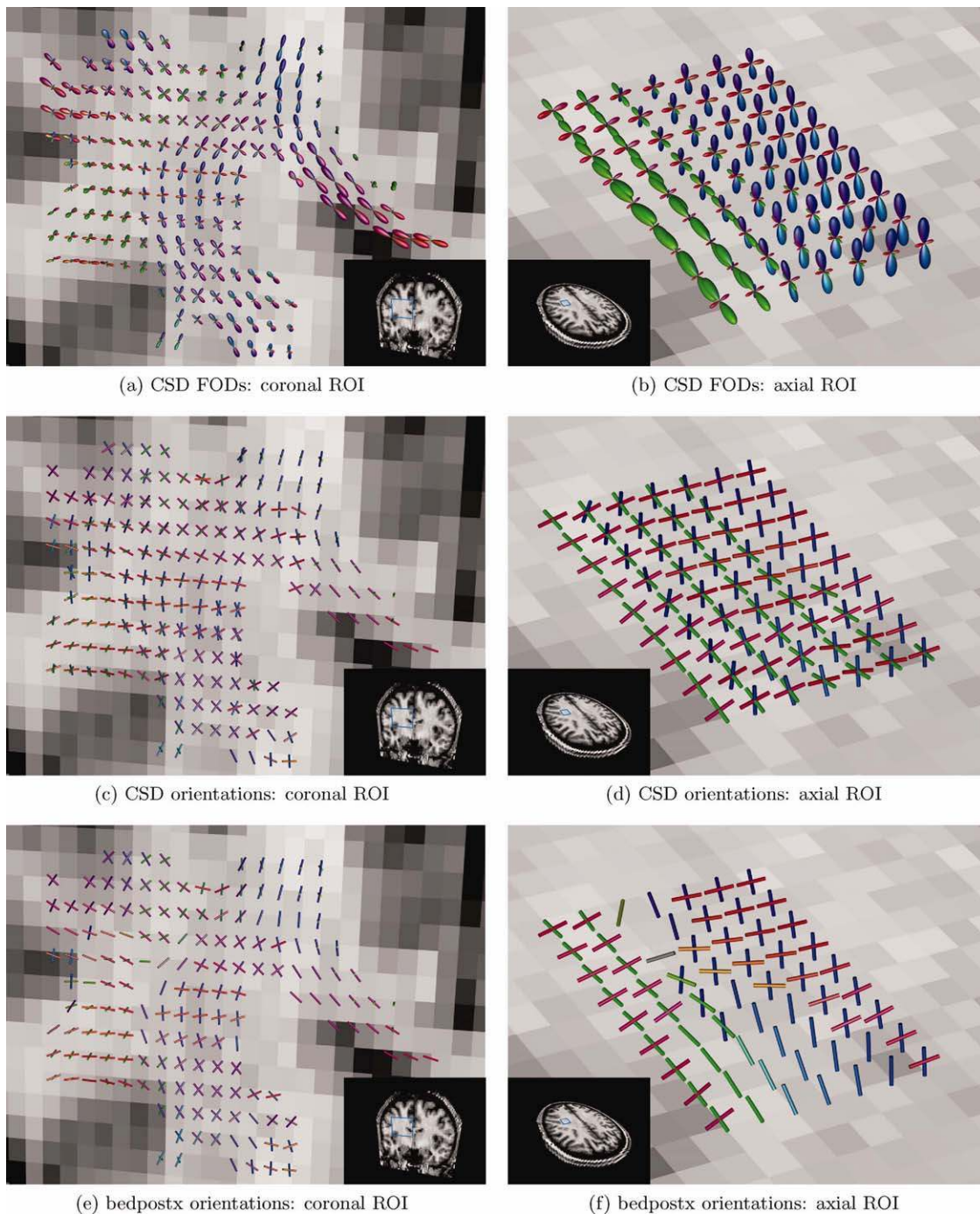
(a) CSD FODs: coronal ROI

(b) CSD FODs: axial ROI

(c) CSD orientations: coronal ROI

(d) CSD orientations: axial ROI

(e) bedpostx orientations: coronal ROI

(f) bedpostx orientations: axial ROI

Figure 5.

Examples of the extracted fiber orientations in two regions containing crossing fibers. The CSD FODs and the extracted fiber orientations are shown in (**a**)–(**b**) and (**c**)–(**d**), respectively. The bedpostx fiber orientations are shown in (**e**)–(**f**). [Color figure can be viewed in the online issue, which is available at wileyonlinelibrary.com.]

crossings was detected, presumably due to its better performance in three-fiber cases, as previously shown in Figures 4 and 5. CSD also detects a higher proportion of small interfiber angles, again in line with the simulation results in Figure 4. In both cases, almost all interfiber angles detected are larger than $\sim 40°$, the minimum angle
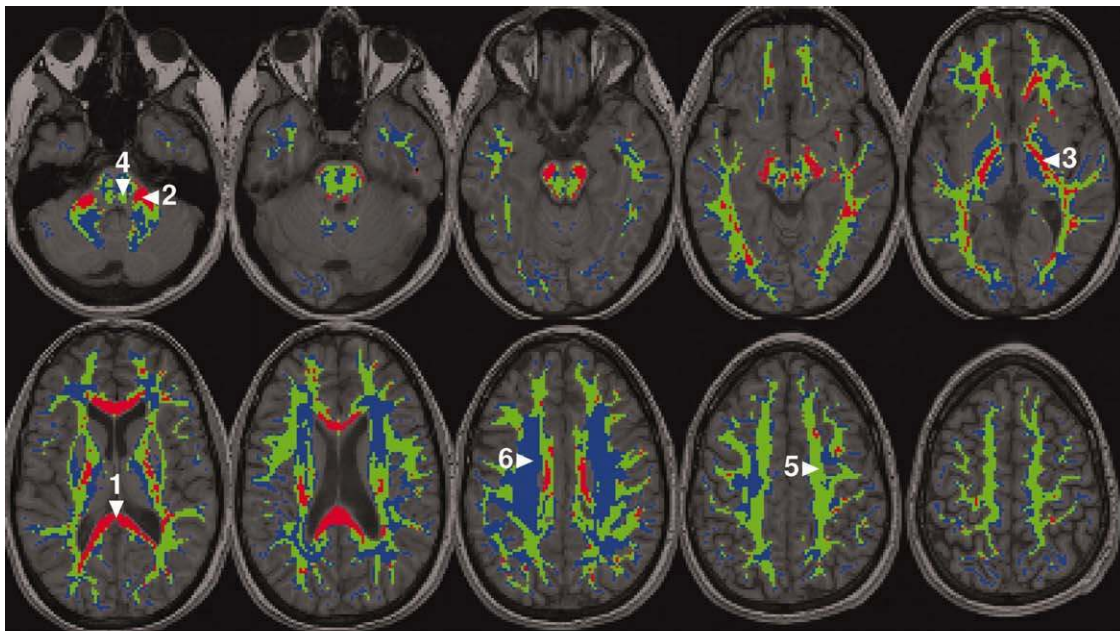
(a) CSD
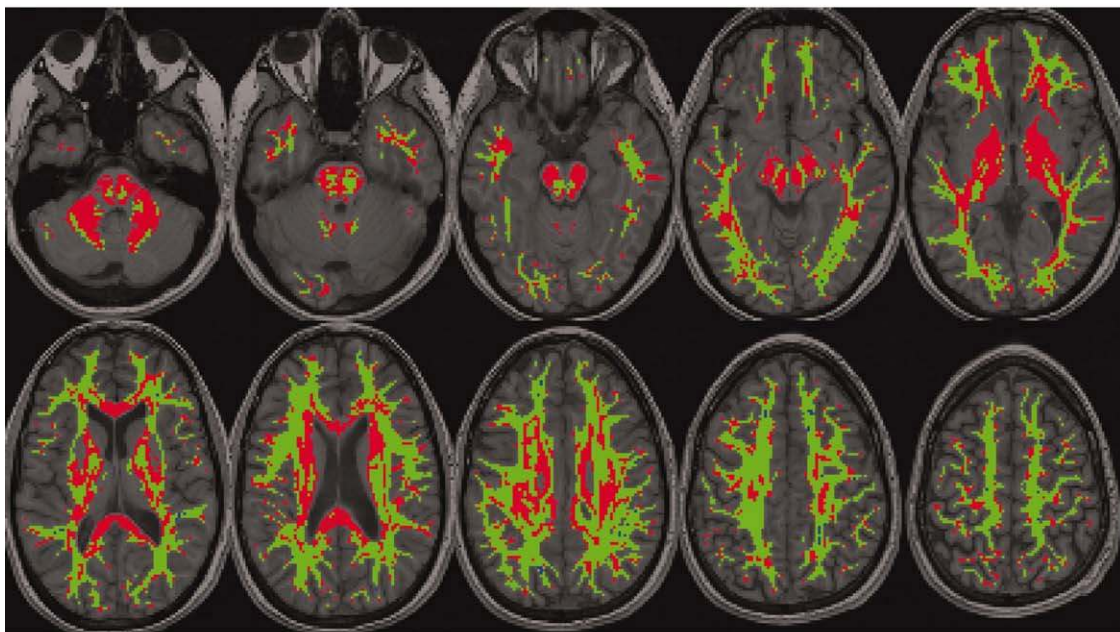
(b) bedpostx

Figure 6.

Number of fiber orientations per voxel (red: 1; green: 2; blue: $\geq$3) for subject 1 estimated with CSD (**a**) and bedpostx (**b**). The numbered arrows in (a) correspond to the following structures: (1) corpus callosum (CC); (2) middle cerebellar peduncle; (3) posterior limb of the internal capsule; (4) pons/motor pathways; (5) superior longitudinal fasciculus (SLF)/corona radiata; (6) corona radiata/SLF/CC. [Color figure can be viewed in the online issue, which is available at wileyonlinelibrary.com.]

that could be resolved by both methods in the simulations. It is likely that smaller crossing angles do exist in the data, but 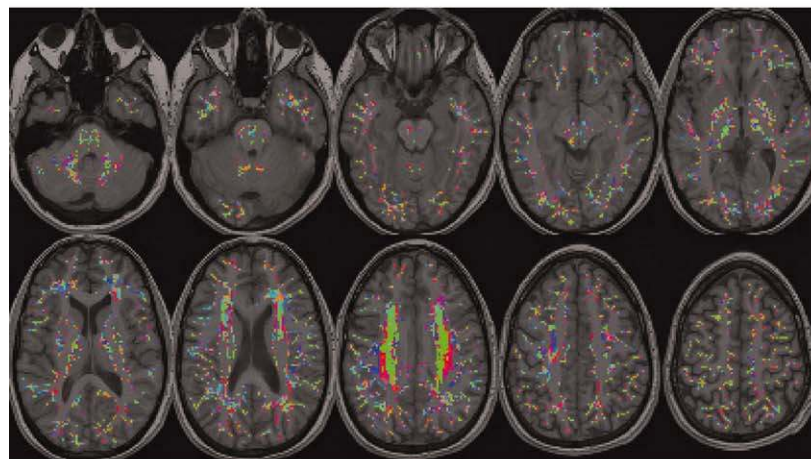cannot be resolved with the methods used. Because these would be labeled as single-fiber voxels, it is likely that the present results underestimate both the extent and the impact of the problem.
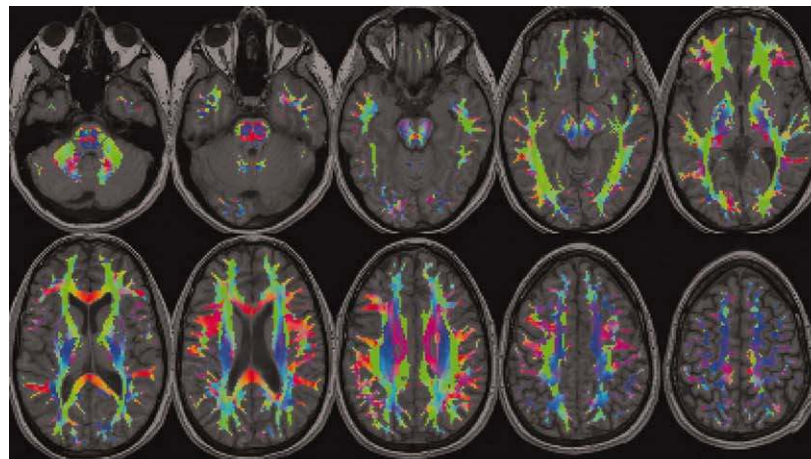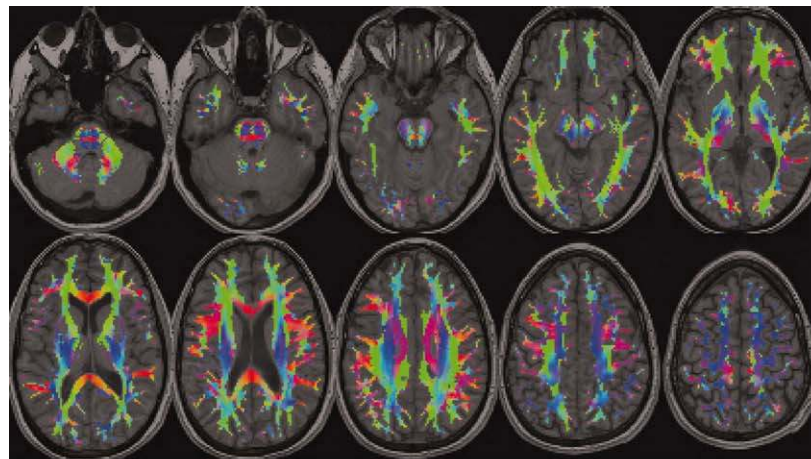
(a) primary fiber orientation
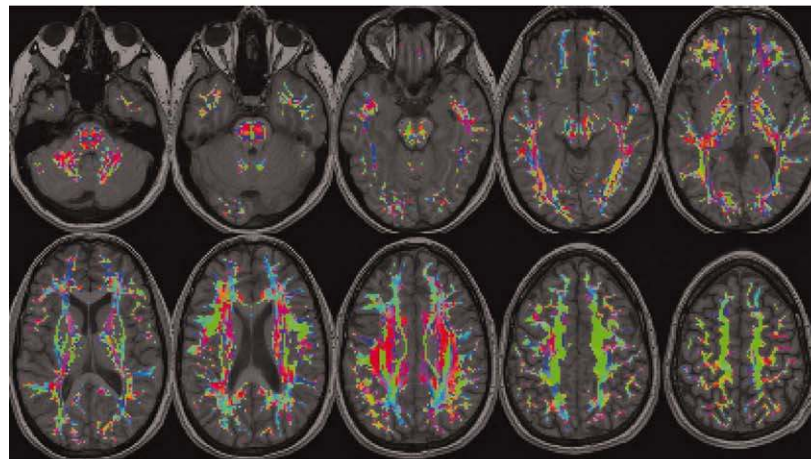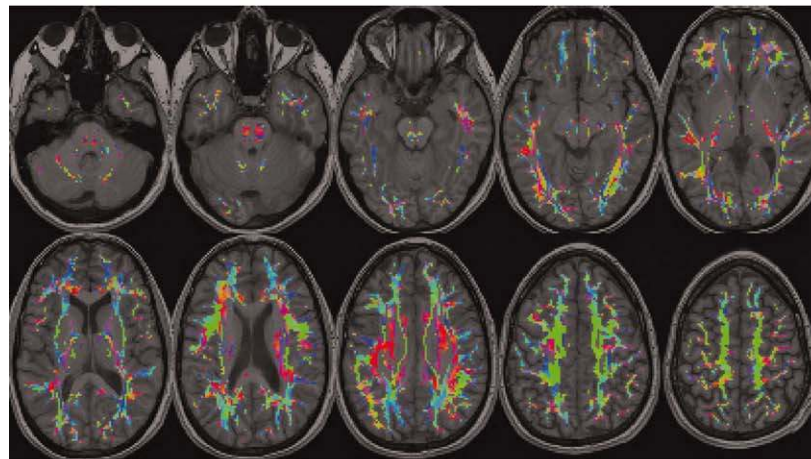
(b) secondary fiber orientation
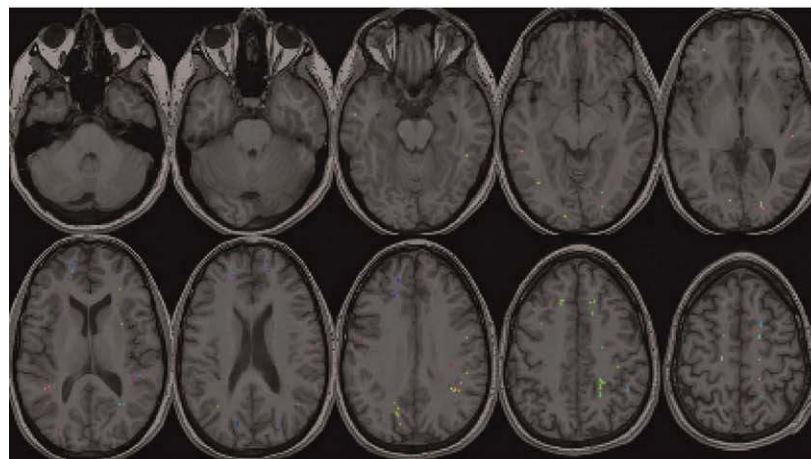
(c) tertiary fiber orientation

Figure 7.

The primary (**a**), secondary (**b**), and tertiary (**c**) fiber orientations (in order of decreasing FOD amplitude) extracted for subject 1 with CSD, shown as RGB color maps (red, left–right; green, anterior–posterior; blue, inferior–superior). [Color figure can be viewed in the online issue, which is available at wileyonlinelibrary.com.]

(a) primary fiber orientation

(b) secondary fiber orientation

(c) tertiary fiber orientation

Figure 8.
The primary (**a**), secondary (**b**), and tertiary (**c**) fiber orientations (in order of decreasing volume fraction) extracted for subject 1 with bedpostx, shown as RGB color maps (red, left–right; green, anterior–posterior; blue, inferior–superior). [Color figure can be viewed in the online issue, which is available at wileyonlinelibrary.com.]

TABLE I. Percentages of single and multifiber voxels throughout the WM for CSD and bedpostx and for different subjects
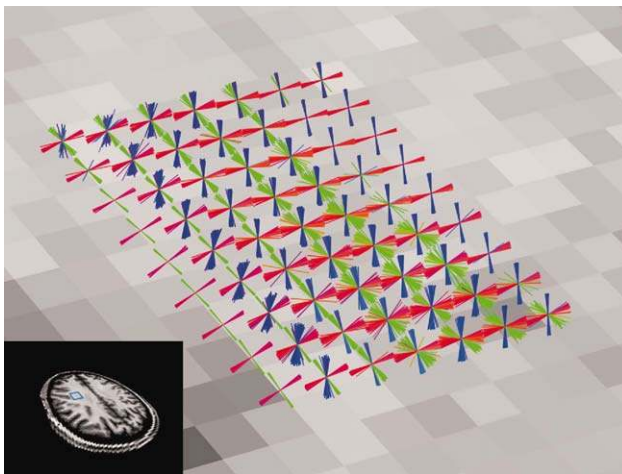
	No. of orientations	1	2	≥3	≥2
CSD	Subject 1	9.5%	47.1%	43.3%	**90.5%**
	Subject 2	8.4%	45.0%	46.6%	**91.6%**
bedpostx	Subject 1	36.1%	62.9%	0.9%	**64.0%**
	Subject 2	37.5%	61.9%	0.4%	**62.3%**
Behrens et al. [2007]		~ 67.7%	~ 33.3%	0%	**~ 33%**

For reference, we also included the estimates previously reported in Behrens et al. [2007].

Assessment of Impact on DTI

The practical implications of these findings for tractography can be appreciated from Figure 13. The fiber orientations estimated using the tensor model and the nearest CSD peak are consistent only in single-fiber regions (e.g., CC). In multifiber regions, the average angular error is ~ 11°. In half of all WM voxels, the angular error is greater than 8° (Fig. 13b,c).

The practical impact of these findings for anisotropy analyses can be appreciated from Figure 14. Most WM voxels contain contributions from nondominant fiber orientations that would be sufficiently large to affect tensor-derived measures of anisotropy (as well as radial and axial diffusivities [Wheeler-Kingshott and Cercignani, 2009]). For example, if we assume that a nondominant partial volume fraction greater than 25% is sufficient to influence anisotropy measures significantly, our results show that 75% of all WM voxels would be affected (Fig. 14b,c). Con-

versely, it can be seen that half of all WM voxels contain more than 40% contamination from crossing fibers.

DISCUSSION

The aim of this study was to provide a more accurate estimate of the extent and impact of the crossing fiber problem in DW–MRI. Using CSD, we observed multiple fiber orientations in ~ 90% of all WM voxels, a much higher proportion than previously reported. With bedpostx, multiple fiber orientations were detected in ~ 63% of all WM voxels, again a much higher proportion than the value of 33% previously reported using the same algorithm, as discussed below [Behrens et al., 2007].

Implications for DTI

The impact of these findings for DTI is profound, particularly for tensor-based tractography, but also for tensor-derived scalar measures. It is widely acknowledged that the fiber orientation estimated using the primary eigenvector of the diffusion tensor will be erroneous in crossing fiber voxels and that these errors will introduce some degree of corruption in the estimated WM pathways [Jones, 2010]. However, until now, the proportion of WM voxels affected by crossing fiber effects was often assumed to be relatively small. Our results clearly indicate that this assumption is not valid. With such a high proportion of

Figure 9.
Consistency of the orientations across residual bootstrap realizations, for the same region as Figure 5d. To aid visualization, only 30 realizations are shown. [Color figure can be viewed in the online issue, which is available at wileyonlinelibrary.com.]
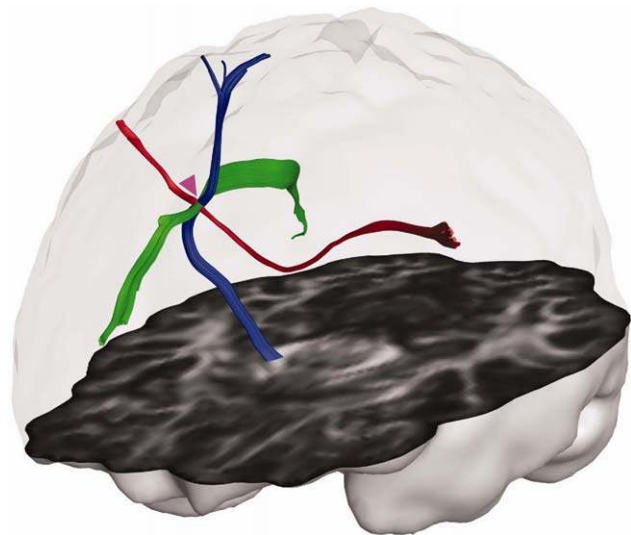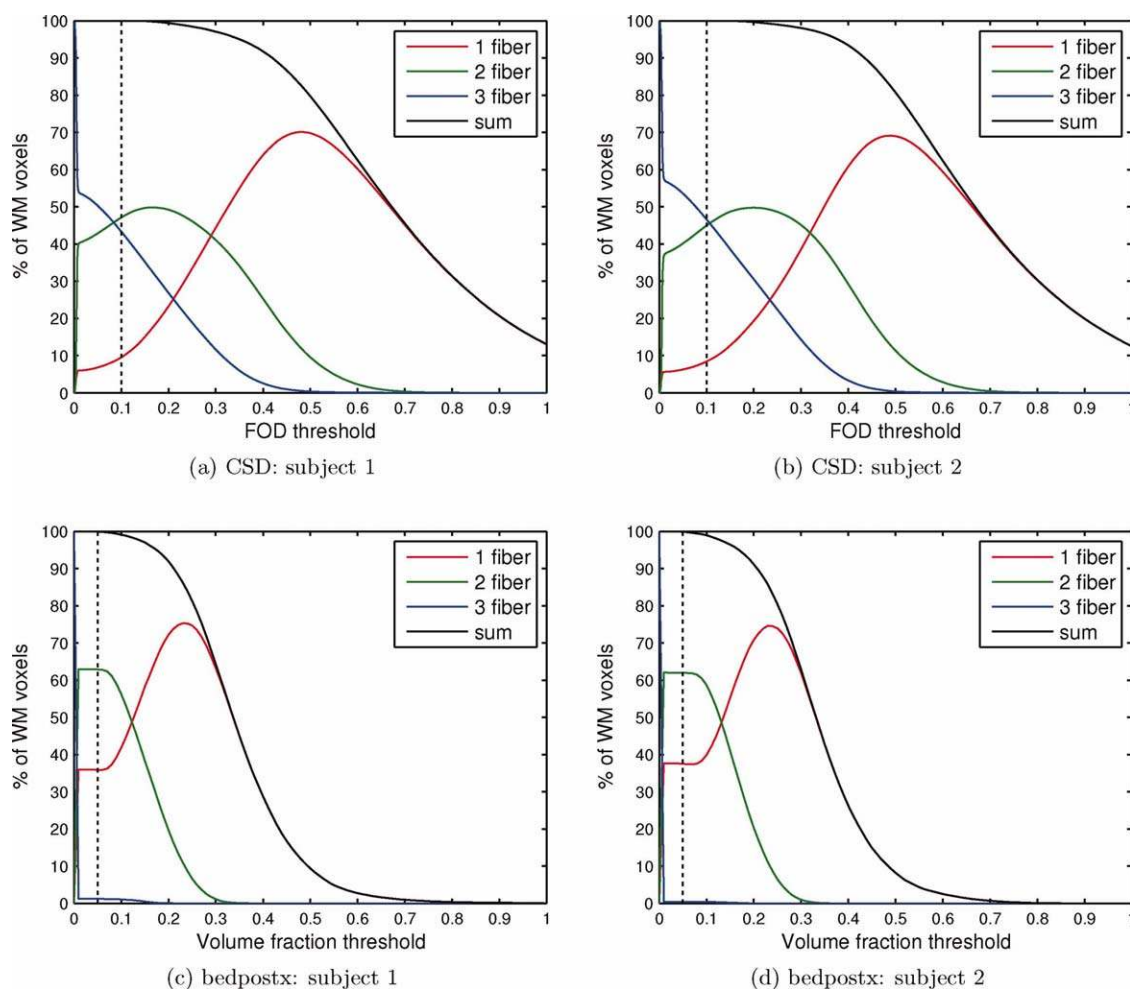

Figure 10.
Tractography in a three-fiber region reveals global consistency of three-fiber orientations. Seed region is indicated by a magenta arrowhead. Commissural fibers are colored red, association fibers green, and projection fibers blue. All three pathways identified using CSD tracking are anatomically plausible. [Color figure can be viewed in the online issue, which is available at wileyonlinelibrary.com.]

Figure 11.

Percentages of single- and multifiber voxels throughout the WM for different CSD FOD thresholds (**a**)–(**b**) and bedpostx volume fraction thresholds (**c**)–(**d**) for both subjects. The actual threshold values used in this study are shown as a dashed line. [Color figure can be viewed in the online issue, which is available at wileyonlinelibrary.com.]

WM voxels containing multiple fiber orientations, it is very unlikely that any WM tract will remain entirely within single-fiber voxels over its entire path. Indeed, as shown in Figure 13, errors in the estimated fiber orientations are widespread throughout the WM: in over half the WM, these errors are larger than 8°. It follows that these errors will adversely and significantly affect the delineation of WM tracts and lead to large numbers of both false-positive and negative results as the tracking algorithm veers off-course, away from the true end-point of the WM tract (false negatives [Behrens et al., 2007; Jeurissen et al., 2011]) and/or into adjacent yet unrelated WM tracts (false positives [Jeurissen et al., 2011; Pierpaoli et al., 2001]). Moreover, it should be emphasized that these errors are provided with respect to the nearest fiber orientation; errors with respect to other fiber orientations that might be present will obviously be considerably greater.

In addition, it is well known that tensor-derived measures of so-called WM integrity, such as FA, as well of other indices such as axial and radial diffusivity, all of which are currently widely used, become ambiguous in these regions [Jones and Cercignani, 2010; Wheeler-Kingshott and Cercignani, 2009]. In Pierpaoli et al. [2001], it was shown that Wallerian degeneration can lead to *increased* diffusion anisotropy in the rostral pons, where transverse pontine fibers are crossing the descending motor pathways. Wallerian degeneration of the motor pathways causes the transverse pontine fibers to become the dominant pathway, and, paradoxically, the measured diffusion anisotropy can increase, because fibers are now more coherently oriented within the voxel. In another study, choice reaction time of healthy volunteers was found to be *positively* correlated with FA [Tuch et al., 2005]. The myelin hypothesis would predict a negative correlation between reaction time and FA,
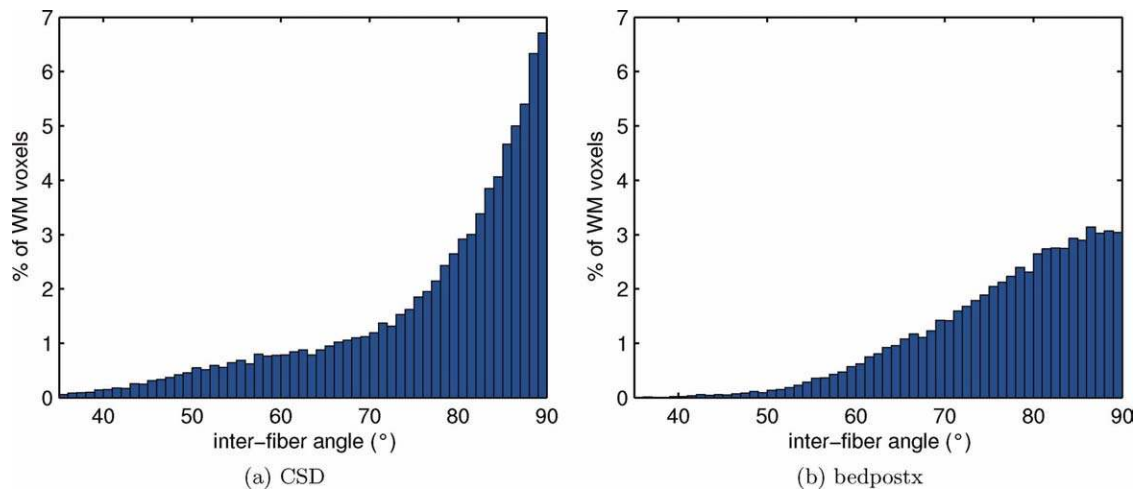
Figure 12.

Histogram of the average interfiber angle for all voxels with ≥ 2 fiber populations for both CSD (**a**) and bedpostx (**b**). [Color figure can be viewed in the online issue, which is available at wileyonlinelibrary.com.]

because increased myelin thickness would cause increased FA and faster nerve conduction velocity, which would in turn result in a shorter reaction time. However, in regions containing multiple fiber orientations, increased FA of an individual fiber population can result in a decrease in the overall FA. In yet another study, *increased* diffusion anisotropy was measured in the centrum semiovale of patients with mild cognitive impairment and mild Alzheimer's disease [Douaud et al., 2011]. This was explained by a relative preservation of motor-related projection fibers crossing with the association fibers of the SLF. These examples show that while tensor-derived indices are highly *sensitive* to changes in the underlying tissue diffusion, their *specificity* in terms of biological interpretation is very ambiguous as any observed changes can also be explained by fiber crossings.

Note that this does not imply that DTI analyses are "wrong" in themselves. Assuming that the DTI analysis was performed well, avoiding all the known pitfalls [Jones and Cercignani, 2010], an observed change in FA is highly likely to correspond to a true underlying biophysical phenomenon. The issue arises from the usual practice of interpreting FA a marker of WM integrity. As illustrated by the examples, in the presence of crossing fibers, the interpretation of increases (or decreases) in FA become highly ambiguous, as they can correspond to either increased or decreased WM integrity or indeed to changes in the relative volume fractions of the various fiber populations. As shown in Figure 14, the proportion of WM voxels where these measures are expected to be significantly confounded is of the order of 75%; given that the interpretation commonly ascribed to these measures is only valid in single-fiber regions, this implies that there are very few regions of brain WM where these measures (including FA and radial/axial diffusivities) can reliably be interpreted as markers of "WM integrity."

Although the data used in this study are of much higher quality than would typically be acquired, it is important to emphasize that these "crossing fiber" issues will still be present to the same extent in any DW–MRI data set. With lower quality data, the power to detect WM voxels containing complex configurations would undeniably be lower, and the estimated proportion of affected voxels would most likely be lower than that reported here. However, while the statistical power to detect multiple fiber orientations would be lower, these multifiber voxels are nonetheless present in the data. Clearly, the impact on tensor-derived estimates of orientation, anisotropy, or radial/axial diffusivity would be identical, with the only difference being noisier estimates.

Robustness of Approach

Given the importance of these findings, great care was taken to ensure the robustness of our results and particularly to avoid any overestimation of the number of fiber orientations. In particular,

- For each subject, we collected 720 DW images, 12 times the amount of data collected in Behrens et al. [2007]. With such a large data set, a higher reliability can be achieved for any subsequent analysis than with a traditional scan consisting of ~ 60 DW images [Jones, 2004].
- Cardiac motion causes local misregistrations of the DW images [Jones and Pierpaoli, 2005; Pierpaoli et al., 2003; Skare and Andersson, 2001], and local signal attenuation in voxels affected by pulsatile motion [Atkinson et al., 2006; Walker et al., 2011]. Both effects could potentially lead to artifactual fiber orientations being detected inside WM voxels. To avoid such pulsation artifacts, cardiac gating was applied [Jones and Cercignani, 2010].
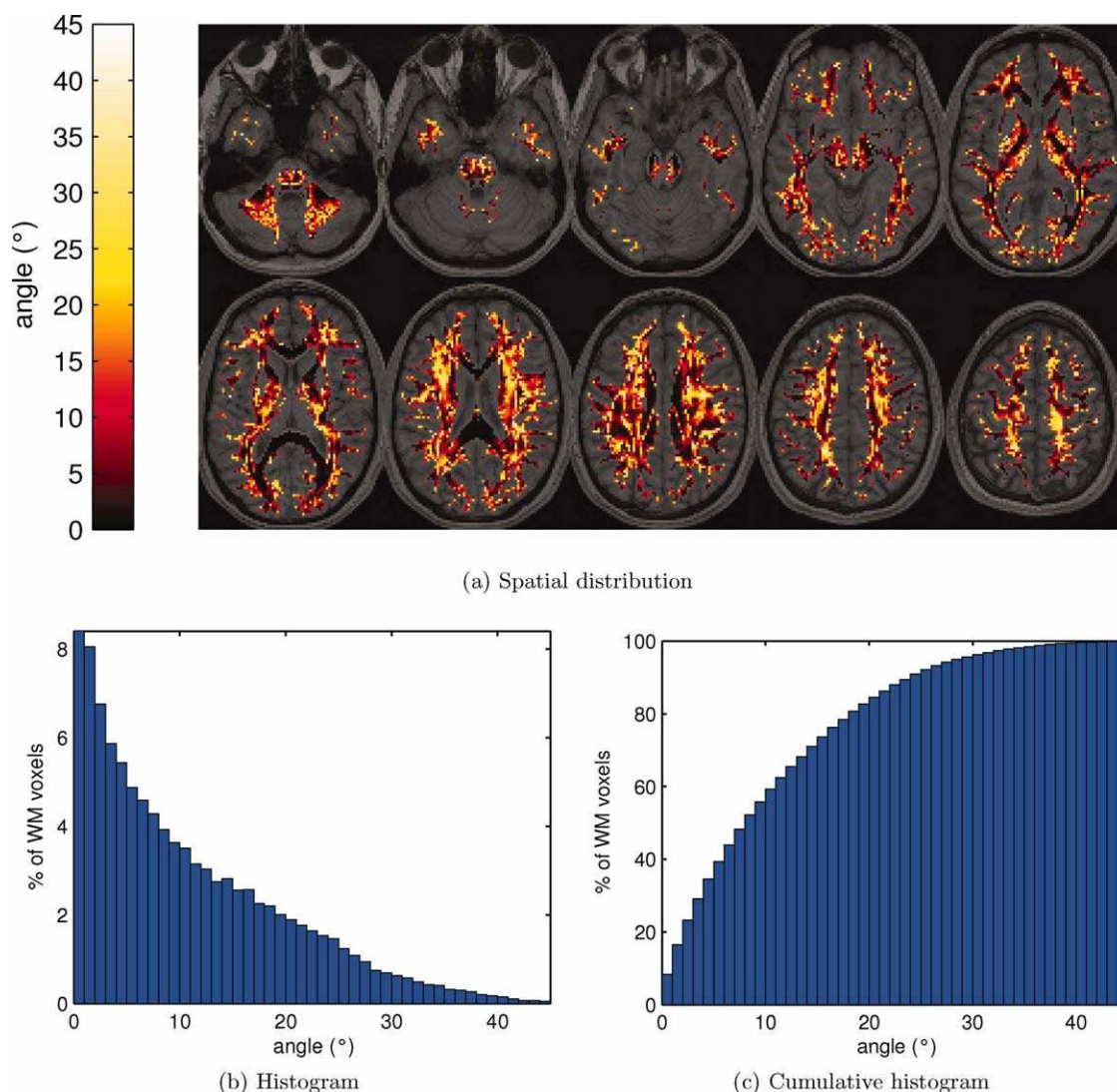
(a) Spatial distribution

(b) Histogram

(c) Cumulative histogram

Figure 13.

The angle between the fiber orientation estimated by the primary eigenvector from DTI and the nearest CSD fiber orientation (**a**) displayed overlaid on an anatomical reference image, (**b**) as a histogram over all WM voxels, and (**c**) as the corresponding cumulative histogram. [Color figure can be viewed in the online issue, which is available at wileyonlinelibrary.com.]

- Head motion and eddy currents cause global misregistration of the DW images, which could also introduce artifactual multifiber voxels due to the mixing of fiber bundles with different orientations. We therefore corrected for subject motion and eddy current distortions, including the required B-matrix adjustments [Leemans and Jones, 2009] and appropriate modulation of the DW images with the Jacobian of the transformation matrix [Jones and Cercignani, 2010].
- Previous studies have used an FA threshold to select WM voxels [Behrens et al., 2007], a method very likely to include both false positives (some GM voxels may

have FA > 0.1) and false negatives (three-fiber WM voxels may have FA < 0.1). To avoid such issues, an objective WM selection method was used based on the corresponding T_1-weighted images (Fig. 2).
- Extensive simulations were performed using parameters *derived from the real data* to carefully tune the FOD threshold and the ARD weight (Fig. 3). Note that we opted for specificity over sensitivity and selected very conservative thresholds.

In this study, we used a *b*-value of 1200 s/mm^2. Although this can be considered relatively low for HARDI
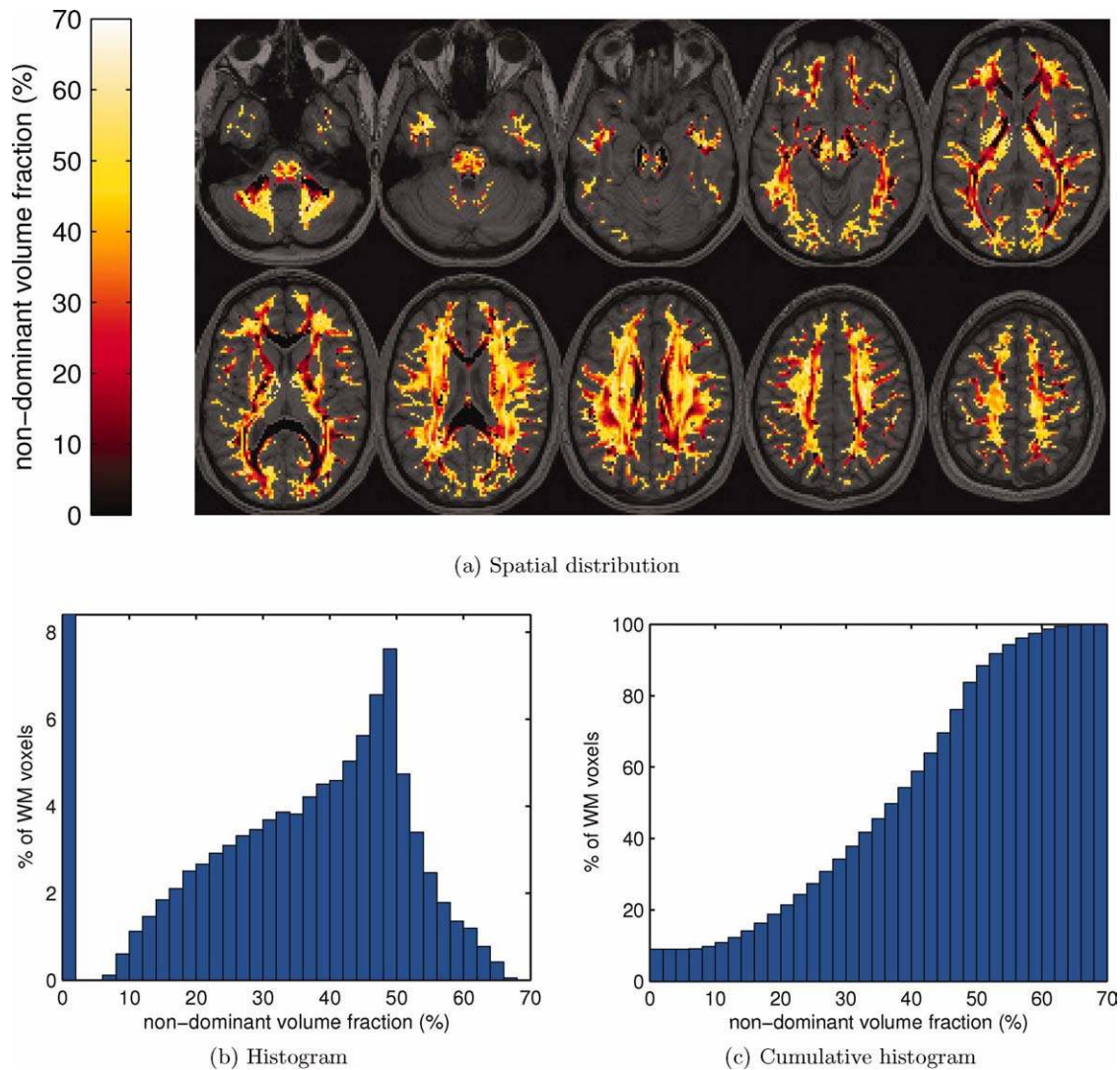
(a) Spatial distribution

(b) Histogram

(c) Cumulative histogram

Figure 14.

The nondominant volume fraction measured by CSD, (**a**) displayed overlaid on an anatomical reference image, (**b**) as a histogram over all WM voxels, and (**c**) as the corresponding cumulative histogram. [Color figure can be viewed in the online issue, which is available at wileyonlinelibrary.com.]

reconstruction methods, this b-value corresponds to what most diffusion MRI studies are currently using [Jones et al., 1999], and our findings are therefore relevant for the vast majority of current DW–MRI studies. However, a consequence of this relatively low-b-value is that the minimum angle that can resolved reliably is limited to $\sim 55°$ using our method (Fig. 4). The practical consequence is that fiber orientations with an interfiber angle smaller than $55°$ will tend to merge into one (average) fiber orientation, making overestimation of the number of fiber orientations very unlikely. Additionally, it shows that even at b-values used in common practice, multifiber voxels can be detected in a large extent of the WM. In the absence of noise and artifacts, performing the same experiment with increased b-values would likely increase the ability of both CSD and bedpostx to resolve smaller interfiber angles [Alexander and Barker, 2005; Behrens et al., 2007; Tournier et al., 2007]. However, at high-b-values, the reduced SNR of the DW images makes it difficult to use registration-based motion and eddy current correction techniques. Given the long scan time used in this study, robust motion correction was deemed imperative, and a more moderate b-value was therefore chosen.

In this study, we did not specifically investigate voxels with more than three fiber orientations, as the volume fractions of the constituent fiber bundles would become

very small and result in small corresponding FOD peak amplitudes in the CSD case (this is not an issue for bedpostx, because it rarely reported more than two-fiber orientations). A very small FOD threshold would be required to detect such small FOD peaks, increasing the risk of introducing false positives (Fig. 3a). Furthermore, as the number of fiber orientations increases, the angle between them will tend to decrease. This will cause many of these fiber orientations to merge (Fig. 4). Nonetheless, we emphasize that this maximum of three-fiber orientations per voxel does not influence the results for the lower orientation counts, because the FOD estimated by CSD is independent of this parameter; it is only used in the subsequent step to select the three largest peaks in the FOD.

A further issue relates to the fact that "bending" and "fanning" configurations contain a range of fiber orientations, which cannot be adequately described using a single discrete number. Nonetheless, while these configurations do not contain "crossing fibers" as such, it is clear that they can only be labeled as containing multiple fiber *orientations*. In this study, the FOD estimated for such configurations will tend to contain a single peak when the curvature remains relatively small or multiple distinct peaks when the curvature is sufficiently large. From this point of view, it is clear that our approach remains conservative.

The voxel size used in this study was 2.4 × 2.4 × 2.4 mm³, a value typical of the DTI literature. This value was chosen, because the primary focus of this study was to estimate the extent and impact of the crossing fiber problem given currently established data acquisition parameters. From a theoretical perspective, increasing spatial resolution has the potential to resolve a proportion of voxels where multiple coherent fiber bundles "brush," that is at the interface between coherent fiber bundles. However, it should be noted that some voxels will always be located at the interface between bundles and will therefore still contain crossing fibers. Furthermore, increasing the resolution will not resolve cases where individual axons of multiple fiber bundles "interdigitate," unless the resolution is increased to the level of the axonal diameter (i.e., of the order of 1 μm), which is clearly impossible with current technology. Consequently, while increasing the resolution may reduce the incidence of multifiber voxels to some extent, it will not remove the problem altogether. From a practical perspective, increasing the spatial resolution is a challenging task. For example: simply reducing the voxel size from 2.4 × 2.4 × 2.4 mm³ to 2 × 2 × 2 mm³ would almost halve the SNR, which can only be recovered by acquiring four signal averages, whilst requiring an increased number of slices to achieve the same spatial coverage. The corresponding increase in scan time required by such an approach is clearly not practical for the vast majority of diffusion studies.

As shown in Figure 5, the fiber orientations extracted using CSD are very consistent with the surrounding orientations, supporting genuine anatomical structures. The same can be deduced from the highly clustered and smoothly transitioning color-encoded orientation maps in Figures 7 and 8 and from the anatomically plausible fiber tracking results in Figure 10. Moreover, by repeating the experiment on a large collection of residual bootstrap realizations and on a different subject, we have shown that our results are consistent both across noise realizations of the same data set (Fig. 9) and across subjects (Table I and Supporting Information).

The full course of the relationship between the FOD threshold and the number of WM voxels with multiple fiber orientations can be seen in Figure 11a,b. Even using an extremely conservative threshold of 0.2, multiple fiber orientations are still found in ∼ 78% of all WM voxels. Further increasing the threshold will result in many small fiber populations being discarded and the introduction of WM voxels without any fiber orientation. Figure 11c,d shows the relationship between the bedpostx volume fraction threshold and the number of WM voxels with multiple fiber orientations. In the range of [0.01–0.1], the number of fiber orientations reported by the bedpostx method is stable, indicating that the ARD has indeed forced compartments to zero, for which it believed that evidence was not sufficiently strong. Starting from a threshold of 0.1, small secondary volume fractions are being discarded, increasing the number of single-fiber voxels and introducing WM voxels without any fiber orientation.

Differences Between CSD and Bedpostx

The two methods used in this study, CSD and bedpostx, provided very different results. These differences can be explained by the simulation results shown in Figure 4 and the in vivo results in Figure 5: in voxels containing 3 fiber orientations, bedpostx will instead report one or two-fiber orientations. Note that the original authors of the ARD method also reported similar limitations [Behrens et al., 2007]. This explains both the increase in one and two-fiber voxels and the relative absence of 3 fiber voxels in the bedpostx results, ultimately resulting in a lower percentage of multifiber voxels.

The large difference between the bedpostx results in this study (63% multifiber voxels) and the bedpostx results from the original study conducted by Behrens et al. [2007] (33% multifiber voxels) can be attributed mostly to the use of a much larger number of DW images, increasing the effective SNR of our data sets: improving SNR will increase the model evidence for smaller fiber volume fractions, resulting in a larger number of significant fiber orientations. In addition, in this study, the ARD weight was tuned specifically to our data, and a longer "burn-in" (a tunable parameter in bedpostx) was used to ensure convergence. Additionally, Behrens et al. [2007] used an FA threshold to select WM voxels, implicitly assuming that all voxels with FA > 0.1 are considered WM, possibly excluding multifiber voxels on account of being too isotropic, introducing a bias toward low-orientation counts. In

addition, low-FA values can become unreliable in the presence of noise [Jones and Cercignani, 2010]. To avoid such issues in our study, an objective WM selection method was used based on the corresponding T_1-weighted images (Fig. 1).

Toward New Measures of WM "Integrity"

An interesting alternative approach to tensor-based scalar metrics is to use the volume fractions as identified by mixture model approaches (such as, for instance, bedpostx and CSD) as a quantitative index. Jbabdi et al. [2010] make tract-wise comparisons directly on the volume fractions as obtained with bedpostx, assuming that increased volume fractions correspond to an increased axonal density along the corresponding fiber orientation. Raffelt et al. [2012] use the FOD derived with spherical deconvolution and make voxel-wise comparisons directly on the full FOD. Their measure, dubbed "apparent fiber density" (AFD) assumes that any differences in the FOD amplitude along a given orientation can be attributed to differences in the relative amount of underlying axons thought to be aligned with this orientation. Recent advances allow nonlinear registration of FOD images [Raffelt et al., 2011], including appropriate reorientation and modulation, thus enabling group comparisons of AFD between patients and controls. While DTI offers an ambiguous average scalar metric for the entire voxel, these new methods provide directionally dependent metrics, which can be associated with individual fiber tracts, providing more specific and more readily interpretable results.

CONCLUSION

In this work, we investigated the prevalence of complex fiber configurations in WM tissue with diffusion MRI. Our results indicate that multiple fiber orientations can be found in a much higher percentage of WM voxels (∼ 90%) than previously reported, with CSD providing much higher estimates than bedpostx. These findings have obvious and profound implications for both tractography and anisotropy analyses and strengthen the growing awareness that fiber tractography and "WM integrity" metrics derived from DTI need to be interpreted with extreme caution.

ACKNOWLEDGMENTS

REFERENCES

Alexander AL, Hasan KM, Lazar M, Tsuruda JS, Parker DL (2001): Analysis of partial volume effects in diffusion-tensor MRI. Magn Reson Med 45:770–780.

Alexander DC (2006): Multiple-fiber reconstruction algorithms for diffusion MRI. Ann NY Acad Sci 1064:113–133.

Alexander DC, Barker GJ, Arridge SR (2002): Detection and modeling of non-Gaussian apparent diffusion coefficient profiles in human brain data. Magn Reson Med 48:331–340.

Ashburner J, Friston KJ (2005): Unified segmentation. NeuroImage 26:839–851.

Assaf Y, Pasternak O (2008): Diffusion tensor imaging (DTI)-based white matter mapping in brain research: A review. J Mol Neurosci 34:51–61.

Atkinson D, Counsell S, Hajnal JV, Batchelor PG, Hill DLG, Larkman DJ (2006): Nonlinear phase correction of navigated multicoil diffusion images. Magn Reson Med 56:1135–1139.

Basser PJ, Mattiello J, LeBihan D (1994a): Estimation of the effective self-diffusion tensor from the NMR spin echo. J Magn Reson Ser B 103:247–247.

Basser PJ, Mattiello J, LeBihan D (1994b): MR diffusion tensor spectroscopy and imaging. Biophys J 66:259–267.

Behrens TEJ, Johansen-Berg H, Jbabdi S, Rushworth MFS, Woolrich MW (2007): Probabilistic diffusion tractography with multiple fibre orientations: What can we gain? NeuroImage 34:144–155.

Ciccarelli O, Catani M, Johansen-Berg H, Clark C, Thompson A (2008): Diffusion-based tractography in neurological disorders: Concepts, applications, and future developments. Lancet Neurol 7:715–727.

Descoteaux M, Deriche R, Knosche TR, Anwander A (2009): Deterministic and probabilistic tractography based on complex fibre orientation distributions. IEEE Trans Med Imag 28:269–286.

Dietrich O, Raya JG, Reeder SB, Reiser MF, Schoenberg SO (2007): Measurement of signal-to-noise ratios in MR images: Influence of multichannel coils, parallel imaging, and reconstruction filters. J Magn Reson Imag 26:375–385.

Douaud G, Jbabdi S, Behrens TEJ, Menke RA, Gass A, Monsch AU, Rao A, Whitcher B, Kindlmann G, Matthews PM, Smith SM (2011): DTI measures in crossing-fibre areas: Increased diffusion anisotropy reveals early white matter alteration in MCI and mild Alzheimer's disease. NeuroImage 55:880–890.

Fillard P, Descoteaux M, Goh A, Gouttard S, Jeurissen B, Malcolm J, Ramirez-Manzanares A, Reisert M, Sakaie K, Tensaouti F, Yo T, Mangin JF, Poupon C (2011) Quantitative evaluation of 10 tractography algorithms on a realistic diffusion MR phantom. NeuroImage 56:220–234.

Frank LR (2001): Anisotropy in high angular resolution diffusion-weighted MRI. Magn Reson Med 45:935–939.

Frank LR (2002): Characterization of anisotropy in high angular resolution diffusion-weighted MRI. Magn Reson Med 47:1083–1099.

Haroon HA, Morris DM, Embleton KV, Alexander DC, Parker GJM (2009): Using the model-based residual bootstrap to quantify uncertainty in fiber orientations from q-ball analysis. IEEE Trans Med Imag 28:535–550.

Jbabdi S, Behrens TEJ, Smith SM (2010): Crossing fibres in tract-based spatial statistics. NeuroImage 49:249–256.

Jeurissen B, Leemans A, Tournier JD, Sijbers J (2009): Fiber tracking on the 'fiber cup phantom' using constrained spherical deconvolution. MICCAI workshop on Diffusion Modelling and

the Fiber Cup (DMFC'09). London, United Kingdom, pp.232–235.

Jeurissen B, Leemans A, Jones DK, Tournier JD, Sijbers J (2011): Probabilistic fiber tracking using the residual bootstrap with constrained spherical deconvolution. Hum Brain Mapp 32:461–479.

Johansen-Berg H, Behrens TEJ (2006): Just pretty pictures? What diffusion tractography can add in clinical neuroscience. Curr Opin Neurol 19:379–385.

Jones DK (2004): The effect of gradient sampling schemes on measures derived from diffusion tensor MRI: A Monte Carlo study. Magn Reson Med 51:807–815.

Jones DK (2008): Studying connections in the living human brain with diffusion MRI. Cortex 44:936–952.

Jones DK (2010): Challenges and limitations of quantifying brain connectivity in vivo with diffusion MRI. Imag Med 2:341–355.

Jones DK, Cercignani M (2010): Twenty-five pitfalls in the analysis of diffusion MRI data. NMR Biomed 23:803–820.

Jones DK, Pierpaoli C (2005): Contribution of cardiac pulsation to variability of tractography results. Proc Intl Soc Magn Reson Med 13:222.

Jones DK, Horsfield MA, Simmons A (1999): Optimal strategies for measuring diffusion in anisotropic systems by magnetic resonance imaging. Magn Reson Med 42:515–525.

Klein S, Staring M, Murphy K, Viergever MA, Pluim JPW (2010): Elastix: A toolbox for intensity based medical image registration. IEEE Trans Med Imag 29:196–205.

Koay CG, Chang LC, Carew JD, Pierpaoli C, Basser PJ (2006): A unifying theoretical and algorithmic framework for least squares methods of estimation in diffusion tensor imaging. J Magn Reson 182:115–125.

Leemans A, Jones DK (2009): The B-matrix must be rotated when correcting for subject motion in DTI data. Magn Reson Med 61:1336–1349.

Leemans A, Sijbers J, Verhoye M, Van der Linden A, Van Dyck D (2005): Mathematical framework for simulating diffusion tensor MR neural fiber bundles. Magn Reson Med 53:944–953.

Leemans A, Jeurissen B, Sijbers J, Jones DK (2009): ExploreDTI: A graphical toolbox for processing, analyzing, and visualizing diffusion MR data. Proceedings of the 17th Scientific Meeting, International Society for Magnetic Resonance in Medicine, Honolulu. p 3537.

Mattes D, Haynor DR, Vesselle H, Lewellyn TK, Eubank W (2001): Nonrigid multimodality image registration. Proc SPIE 4322:1609.

Miller KL, Stagg CJ, Douaud G, Jbabdi S, Smith SM, Behrens TEJ, Jenkinson M, Chance SA, Esiri MM, Voets NL, Jenkinson N, Aziz TZ, Turner MR, Johansen-Berg H, McNab JA (2011): Diffusion imaging of whole, post-mortem human brains on a clinical MRI scanner. NeuroImage 57:167–181

Mori S, van Zijl PCM (2002): Fiber tracking: Principles and strategies—A technical review. NMR Biomed 15:468–480

Mori S, Zhang J (2006): Principles of diffusion tensor imaging and its applications to basic neuroscience research. Neuron 51:527–539.

O'Muircheartaigh J, Vollmar C, Traynor C, Barker GJ, Kumari V, Symms MR, Thompson P, Duncan JS, Koepp MJ, Richardson MP (2011): Clustering probabilistic tractograms using independent component analysis applied to the thalamus. NeuroImage 54:2020–2032.

Pierpaoli C, Barnett A, Pajevic S, Chen R, Penix LR, Virta A, Basser PJ (2001): Water diffusion changes in Wallerian degeneration and their dependence on white matter architecture. NeuroImage 13:1174–1185.

Pierpaoli C, Marenco S, Rohde G, Jones DK, Barnett AS (2003): Analyzing the contribution of cardiac pulsation to the variability of quantities derived from the diffusion tensor. Proceedings of the 11th Scientific Meeting, International Society for Magnetic Resonance in Medicine, Toronto, Canada. p 70.

Raffelt D, Tournier JD, Fripp J, Crozier S, Connelly A, Salvado O (2011): Symmetric diffeomorphic registration of fibre orientation distributions. NeuroImage 56:1171–1180.

Raffelt D, Tournier JD, Rose S, Ridgway GR, Henderson R, Crozier S, Salvado O, Connelly A (2012): Apparent fibre density: A novel measure for the analysis of diffusion-weighted magnetic resonance images. NeuroImage 3976–3994.

Skare S, Andersson JLR (2001): On the effects of gating in diffusion imaging of the brain using single shot EPI. Magn Reson Imag 19:1125–1128.

Stejskal EO, Tanner JE (1965): Spin diffusion measurements: Spin echoes in the presence of a time-dependent field gradient. J Chem Phys 42:288.

Tournier JD, Calamante F, Gadian DG, Connelly A (2004): Direct estimation of the fiber orientation density function from diffusion-weighted MRI data using spherical deconvolution. NeuroImage 23:1176–1185.

Tournier JD, Calamante F, Connelly A (2007): Robust determination of the fibre orientation distribution in diffusion MRI: Non-negativity constrained super-resolved spherical deconvolution. NeuroImage 35:1459–1472.

Tournier JD, Yeh CH, Calamante F, Cho KH, Connelly A, Lin CP (2008): Resolving crossing fibres using constrained spherical deconvolution: Validation using diffusion-weighted imaging phantom data. NeuroImage 42:617–625.

Tournier JD, Mori S, Leemans A (2011): Diffusion tensor imaging and beyond. Magn Reson Med 65:1532–1556.

Tuch DS, Reese TG, Wiegell MR, Makris N, Belliveau JW, Wedeen VJ (2002): High angular resolution diffusion imaging reveals intravoxel white matter fiber heterogeneity. Magn Reson Med 48:577–582.

Tuch DS, Salat DH, Wisco JJ, Zaleta AK, Hevelone ND, Rosas HD (2005): Choice reaction time performance correlates with diffusion anisotropy in white matter pathways supporting visuospatial attention. Proc Natl Acad Sci USA 102:12212.

Vos SB, Jones DK, Viergever MA, Leemans A (2011): Partial volume effect as a hidden covariate in DTI analyses. NeuroImage 55:1566–1576.

Vos SB, Jones DK, Jeurissen B, Viergever MA, Leemans A (2012): The influence of complex white matter architecture on the mean diffusivity in diffusion tensor MRI of the human brain. NeuroImage 59:2208–2216.

Walker L, Chang LC, Koay CG, Sharma N, Cohen L, Verma R, Pierpaoli C (2011): Effects of physiological noise in population analysis of diffusion tensor MRI data. NeuroImage 54:1168–1177.

Wheeler-Kingshott CAM, Cercignani M (2009): About axial and radial diffusivities. Magn Reson Med 61:1255–1260.

Woolrich MW, Jbabdi S, Patenaude B, Chappell M, Makni S, Behrens TEJ, Beckmann C, Jenkinson M, Smith SM (2009): Bayesian analysis of neuroimaging data in FSL. NeuroImage 45:S173–S186.